

Multivalued Geodesic Ray-Tracing for Computing Brain Connections Using Diffusion Tensor Imaging*

N. Sepasian[†], J. H. M. ten Thije Boonkkamp[‡], B. M. Ter Haar Romeny[†], and A. Vilanova[†]

Abstract. Diffusion tensor imaging (DTI) is a magnetic resonance technique used to explore anatomical fibrous structures, like brain white matter. Fiber-tracking methods use the diffusion tensor (DT) field to reconstruct the corresponding fibrous structure. A group of fiber-tracking methods trace geodesics on a Riemannian manifold whose metric is defined as a function of the DT. These methods are more robust to noise than more commonly used methods where just the main eigenvector of the DT is considered. Until now, geodesic-based methods were not able to resolve all geodesics, since they solved the Eikonal equation, and therefore were not able to deal with multivalued solutions. Our algorithm computes multivalued solutions using an Euler–Lagrange form of the geodesic equations. The multivalued solutions become relevant in regions with sharp anisotropy and complex geometries, or when the first arrival time does not describe the geodesic close to the anatomical fibrous structure. In this paper, we compare our algorithm with the commonly used Hamilton–Jacobi (HJ) equation approach. We describe and analyze the characteristics of both methods. In the analysis we show that in cases where, e.g., U-shaped bundles appear, our algorithm can capture the underlying fiber structure, while other approaches will fail. A feasibility study with results for synthetic and real data is shown.

Key words. diffusion tensor imaging, fiber-tracking, Riemannian geometry, geodesics, Euler–Lagrange equations, Hamilton–Jacobi equation

AMS subject classifications. 92C55, 65D17, 68U10

DOI. 10.1137/110824395

1. Introduction. Diffusion tensor imaging (DTI) is the only noninvasive technique that allows the reconstruction of images of brain white matter bundles [2, 34]. Due to the fibrous structure of white matter, diffusion of water molecules is dominant in the direction of the fibers. Diffusion and its directional variation can be measured by diffusion weighed magnetic resonance imaging (DW-MRI). By acquiring DW images in at least six gradient directions, it is possible to estimate a 3×3 positive-definite symmetric second-order tensor, the so-called diffusion tensor [2, 35]. The eigenvector corresponding to the largest eigenvalue of this tensor is considered to point in the direction of the fiber tracts. Numerous algorithms have been introduced for reconstructing the fibrous structure from DTI. In the most commonly used fiber-tracking algorithms, i.e., streamline-based methods, the fibers are estimated by using the principal direction of the diffusion tensor [35]. Here, fiber-tracking stops if there is a sharp

*Received by the editors February 14, 2011; accepted for publication (in revised form) January 12, 2012; published electronically April 4, 2012. This work was supported by The Netherlands Organization for Scientific Research (NWO).

<http://www.siam.org/journals/siims/5-2/82439.html>

[†]Biomedical Technology, Eindhoven University of Technology, 5600 MB Eindhoven, The Netherlands (N.Sepasian@tue.nl, B.M.TerHaarRomeny@tue.nl, A.Vilanova@tue.nl).

[‡]Centre for Analysis, Scientific Computing and Applications, Eindhoven University of Technology, 5600 MB Eindhoven, The Netherlands (J.H.M.tenThijeBoonkkamp@tue.nl).

turn in the trajectory, or when the fiber enters a region of low anisotropy where the main eigenvector cannot be clearly identified. The main eigenvector is not well defined, either due to noise or to the presence of crossing fibers. Furthermore, streamline methods are based on local characteristics and therefore sensitive to noise.

A possible solution for resolving these limitations of classic fiber-tracking is to apply more global approaches such as geodesic-based algorithms [13, 27, 44, 32]. These techniques are based on the assumption that fibers follow the most efficient diffusion propagation paths. A Riemannian manifold is defined using as metric the inverse of the diffusion tensor. Paths on this manifold are shorter if the diffusion is stronger along that path. Therefore geodesics (i.e., shortest paths) on this manifold follow the most efficient diffusion paths. The geodesics are often computed from the stationary Hamilton–Jacobi (HJ) equation. Equidistant fronts are emanating from a certain initial point. The propagation speed of the fronts at each point in space is a local variable. Parker, Wheeler-Kingshott, and Barker [42] presented a similar approach where the local speed was based on a combination of the normal vector and the tensor dominant eigenvector. This approach is prone to incorrect propagation in anisotropic domains. In recent publications [27, 19, 20], front propagation inside anisotropic domains has been considered, which is suitable for oriented domains. The propagation speed of the front is given by the diffusivity rate in the normal direction of the front; the fibers are extracted by back tracing along the characteristics of the front.

One property of solving the HJ equation is that it gives only the single-valued viscosity solution corresponding to the minimizer of the length functional. It is also well known that the solution of the HJ equation can develop discontinuities in the gradient space, cusps. Cusps occur when the correct solution should become multivalued. HJ methods are not able to handle this situation. In this paper, we focus on developing an algorithm that can tackle this shortcoming.

Recently, Sepasian et al. [49, 48] presented a ray-tracing algorithm for computing geodesics in anisotropic domains. They defined the metric as the inverse of the diffusion tensor [13, 27]. In contrast to other geodesic-based methods, this approach can capture multivalued geodesics connecting two given points by considering the geodesics as functions of position and direction. Moreover, it is based on the Euler–Lagrange (EL) equations, and therefore local changes in the geodesic can be taken into account. In [49] Sepasian et al. focused on the mathematical and numerical model for analytic and synthetic fields in two-dimensional domains. In a later paper [48], Sepasian et al. presented the algorithm for the ray-tracing method in three dimensions with some examples of synthetic and brain data. The purpose of the current paper is to provide better insight into details of the ray-tracing algorithm. It presents the differences, advantages, and disadvantages compared to numerical solution of the HJ equation. In addition, we evaluate the algorithm for real brain DTI data, as well as for synthetic crossing fibers.

It should be noted that the methods mentioned until now belong to the class of deterministic fiber-tracking methods; i.e., given the same input, these methods will always give the same result. In the case of geodesic-based methods, given two points in the domain, a finite number of geodesics paths (i.e., one in the case of HJ methods) will be found. Probabilistic fiber-tracking constitutes another class of methods, where the variation of the pathways due to model assumptions and/or noise is considered. A probabilistic distribution is built, and a random process generates many paths originating from one initial position [5, 41, 39, 10, 9, 51].

Then the probability that a fiber originating in that position goes through a given area is determined by the number of random paths that go through that area [40, 18]. Probabilistic methods can use deterministic fiber-tracking methods as part of the process [17, 4, 3, 18, 21].

In this article we focus on deterministic geodesic-based methods. Next, we first describe different mathematical models for computing geodesics and their connections to diffusion tensor (DT) images. Later, we propose numerical methods for solving the equations. Finally, we present results for realistic synthetic data and human brain DTI.

2. Mathematical models. As mentioned in section 1, we assume that fiber tracts coincide with geodesics in the Riemannian manifold defined using the inverse of the DT as metric. The rationale behind this assumption is that water molecules move freely along fiber tracts, and their movement is restricted in the perpendicular direction. Therefore, it is assumed that the fiber connecting two points follows the most efficient diffusion path for water molecules. We are searching for a path that maximizes diffusion. This can be achieved by inverting the metric that makes the largest eigenvalue become the smallest one. Consequently, the geodesic for this metric represents the fibers [56]. In order to construct the geodesics, two different governing equations can be derived. In this section, first we present the EL equations for a specific metric. Next, we formulate the corresponding HJ equation.

Consider a bounded curve \mathcal{C} , with parametrization $\mathbf{x} = \boldsymbol{\chi}(\tau)$, $a \leq \tau \leq b$. A geodesic between two points $\boldsymbol{\chi}(a)$ and $\boldsymbol{\chi}(b)$ is the smooth curve whose length is the minimum of all possible lengths. In the presentation that follows we use the Einstein notation; i.e., we sum over repeated indices, one in the upper (superscript) and one in the lower (subscript) position. Introducing the metric $ds^2 = g_{\alpha\beta} dx^\alpha dx^\beta$, the length of \mathcal{C} is given by

$$(2.1) \quad J[\boldsymbol{\chi}] = \int_{\mathcal{C}} ds = \int_a^b \left(g_{\alpha\beta}(\boldsymbol{\chi}(\tau)) \dot{\chi}^\alpha(\tau) \dot{\chi}^\beta(\tau) \right)^{1/2} d\tau,$$

where $G = (g_{\alpha\beta})$ is the inverse of the diffusion tensor D , i.e., $G = D^{-1}$. Therefore, $(g_{\alpha\beta})$ depends only on \mathbf{x} and is symmetric positive definite. In the following we use the shorthand notation $\dot{x}^\alpha = \dot{\chi}^\alpha(\tau)$.

From calculus of variations, we know that the necessary condition for $\boldsymbol{\chi}(\tau)$ to minimize $J[\boldsymbol{\chi}]$ is the set of EL equations which read [14]

$$(2.2) \quad \frac{\partial L}{\partial x^\alpha} - \frac{d}{d\tau} \left(\frac{\partial L}{\partial \dot{x}^\alpha} \right) = 0,$$

where $L = L(\mathbf{x}, \dot{\mathbf{x}})$ is the Lagrangian corresponding to (2.1) and is given by

$$(2.3) \quad L(\mathbf{x}, \dot{\mathbf{x}}) = \left(g_{\alpha\beta}(\mathbf{x}) \dot{x}^\alpha \dot{x}^\beta \right)^{1/2}.$$

The required derivatives of L are given by

$$\frac{\partial L}{\partial x^\alpha} = \frac{1}{2L} \frac{\partial g_{\beta\gamma}}{\partial x^\alpha} \dot{x}^\beta \dot{x}^\gamma, \quad \frac{\partial L}{\partial \dot{x}^\alpha} = \frac{1}{L} g_{\beta\alpha} \dot{x}^\beta.$$

Next, we take for τ the arc length, i.e., $L = 1$ and $\frac{dL}{d\tau} = 0$ [29]. Substituting the derivatives above into (2.2), we obtain

$$(2.4) \quad g_{\alpha\beta} \ddot{x}^\beta + [\beta\gamma, \alpha] \dot{x}^\beta \dot{x}^\gamma = 0,$$

where $[\beta\gamma, \alpha]$ is the Christoffel symbol of the first kind, given by

$$(2.5) \quad [\beta\gamma, \alpha] = \frac{1}{2} \left(\frac{\partial g_{\alpha\beta}}{\partial x^\gamma} + \frac{\partial g_{\alpha\gamma}}{\partial x^\beta} - \frac{\partial g_{\beta\gamma}}{\partial x^\alpha} \right);$$

see [47, 14]. Multiplying (2.4) with the inverse of the metric $G^{-1} = (g^{\alpha\beta})$, we find

$$(2.6) \quad \ddot{x}^\alpha + \Gamma_{\beta\gamma}^\alpha \dot{x}^\beta \dot{x}^\gamma = 0,$$

where $\Gamma_{\beta\gamma}^\alpha$ is the Christoffel symbol of the second kind, defined by

$$(2.7) \quad \Gamma_{\beta\gamma}^\alpha = g^{\alpha\delta} [\beta\gamma, \delta].$$

In contrast to the functional in (2.1), we now consider the functional that minimizes the length of all curves joining the fixed point $\chi(a)$ and variable end point $\chi(t)$, i.e.,

$$(2.8) \quad T(\mathbf{x}, t) = \min_{\chi} \int_a^t L(\chi(\tau), \dot{\chi}(\tau)) d\tau,$$

with $\mathbf{x} = \chi(t)$ and L given in (2.3). The geodesic connecting $\chi(a)$ with $\chi(t)$ can be determined from the HJ equation, given by

$$(2.9) \quad H\left(\mathbf{x}, \frac{\partial T}{\partial \mathbf{x}}\right) = 1,$$

where the Hamiltonian H is described by [46, 38]

$$(2.10) \quad H^2(\mathbf{x}, \mathbf{p}) = g^{\alpha\beta}(\mathbf{x}) p_\alpha p_\beta, \quad p_\alpha := g_{\alpha\beta}(\mathbf{x}) \dot{x}^\beta.$$

With this choice for the Hamiltonian we obtain the *anisotropic eikonal* equation

$$(2.11) \quad F(x^\alpha, q_\alpha) = g^{\alpha\beta} \frac{\partial T}{\partial x^\alpha} \frac{\partial T}{\partial x^\beta} - 1 = 0, \quad q = \frac{\partial T}{\partial x^\alpha}.$$

We can show that the first-order PDE (2.11) is equivalent to the Charpit system of equations [31], i.e.,

$$(2.12a) \quad \dot{x}^\alpha = \frac{\partial F}{\partial q_\alpha} = g^{\alpha\beta} q_\beta,$$

$$(2.12b) \quad \dot{q}^\alpha = -\frac{\partial F}{\partial x^\alpha} = -\frac{1}{2} \frac{\partial g^{\beta\gamma}}{\partial x^\alpha} q_\beta q_\gamma,$$

$$(2.12c) \quad \dot{T} = q_\alpha \frac{\partial F}{\partial q_\alpha} = g^{\alpha\beta} q_\alpha q_\beta.$$

This seven-dimensional system of ODEs describes the solution of (2.11). Here (2.12a) and (2.12b) are the canonical form of the EL equations [15, 45]. In this way we can reconstruct the geodesics by tracing back the characteristics of the fronts $T(\mathbf{x}, t) = \text{const}$. Note that for an isotropic medium the characteristics are perpendicular to the fronts. For more details we refer the reader to Sethian and Vladimirovsky [50].

The solution of the HJ equation may develop multivalued solutions when two fronts collide, such as focus points, caustics, or discontinuities in the gradient field. Those regions are called *shocks*. Therefore, the viscosity solution is needed to ensure the existence and uniqueness of the solution of (2.11); see, e.g., Mantegazza and Menzucchi [30]. Regardless of the numerical scheme for solving the HJ equation, the solution always satisfies the viscosity solution concepts, and there is always a unique geodesic that connects two given points. Under the viscosity concept T need not be everywhere differentiable, and there may be points where $\frac{\partial T}{\partial x^\alpha}$ does not exist; i.e., there could be a kink in T and yet T satisfies the equation in an appropriate sense [11]. However, using the viscosity solution will not ensure that the solution we obtain is the real physically meaningful one [45].

In DTI fiber-tracking, different methods have been derived based on front propagation in anisotropic fields using the HJ equation [19, 28, 20, 42]. Moreover, it is known that for anisotropic domains, such as in DTI, the more realistic fibers can be reconstructed by back tracing the characteristics rather than gradients of the fronts [19, 50].

Our group [49, 48] introduced an algorithm based on the ray-tracing method for geodesic fiber-tracking. In this approach, all arrival times of the fronts are considered, rather than only the first arrival time at each grid point. The major advantage of this approach is the capacity to capture possible multipath connections between two given points. This is an advantage because in ray-tracing we do not constrain the solution to the viscosity solution; instead, at each grid point, we can get many possible arrival times. Therefore, the ray-tracing method can better simulate the correct solution. Figure 1 shows the difference between the solutions of ray-tracing, the eikonal equation, and wave front propagation for anisotropic media with one source. Wave propagation in anisotropic media, as it occurs in DTI fields, creates shocks (see Figure 1(a)). It has been shown that one can reconstruct wave fronts that evolve according to rays [6, 45]. In contrast to the fronts obtained by solving the HJ equation (see Figure 1(b)), the wave fronts obtained by ray-tracing maintain the corresponding topology once the multivalued solution occurs (see Figure 1(c)). It can be observed that the eikonal solution in Figure 1(b) fails to reproduce the real front solution, while ray-tracing is able to grasp the complex multivalued solutions in Figure 1(c). Wave front construction becomes very complex and computationally expensive for fields with complex topology in comparison with the ray-tracing method.

3. Numerical methods. In this section we focus on constructing numerical schemes for computing the geodesics using the geodesic equations (2.6) or the HJ equation (2.11). First, we present the so-called ray-tracing method for reconstructing fiber tracts in a three-dimensional Riemannian space. Subsequently, we explain the fast sweeping algorithm for computing the solution of the HJ equation that we use for comparison.

3.1. Ray-tracing. Ray-tracing refers to methods for calculating the trajectory of waves or particles passing through a domain with regions of varying propagation velocity. This affects the resulting propagation wavefront topologies such that they may bend or change direction. Ray-tracing assumes that the particle or wave can be modeled as a large number of very narrow bundles of rays, and for a very small distance a ray is locally straight. The ray-tracing procedure constructs the ray over this distance. In order to estimate the ray's new direction, a local derivative of the medium is used. From the new location, a new ray is traced, and

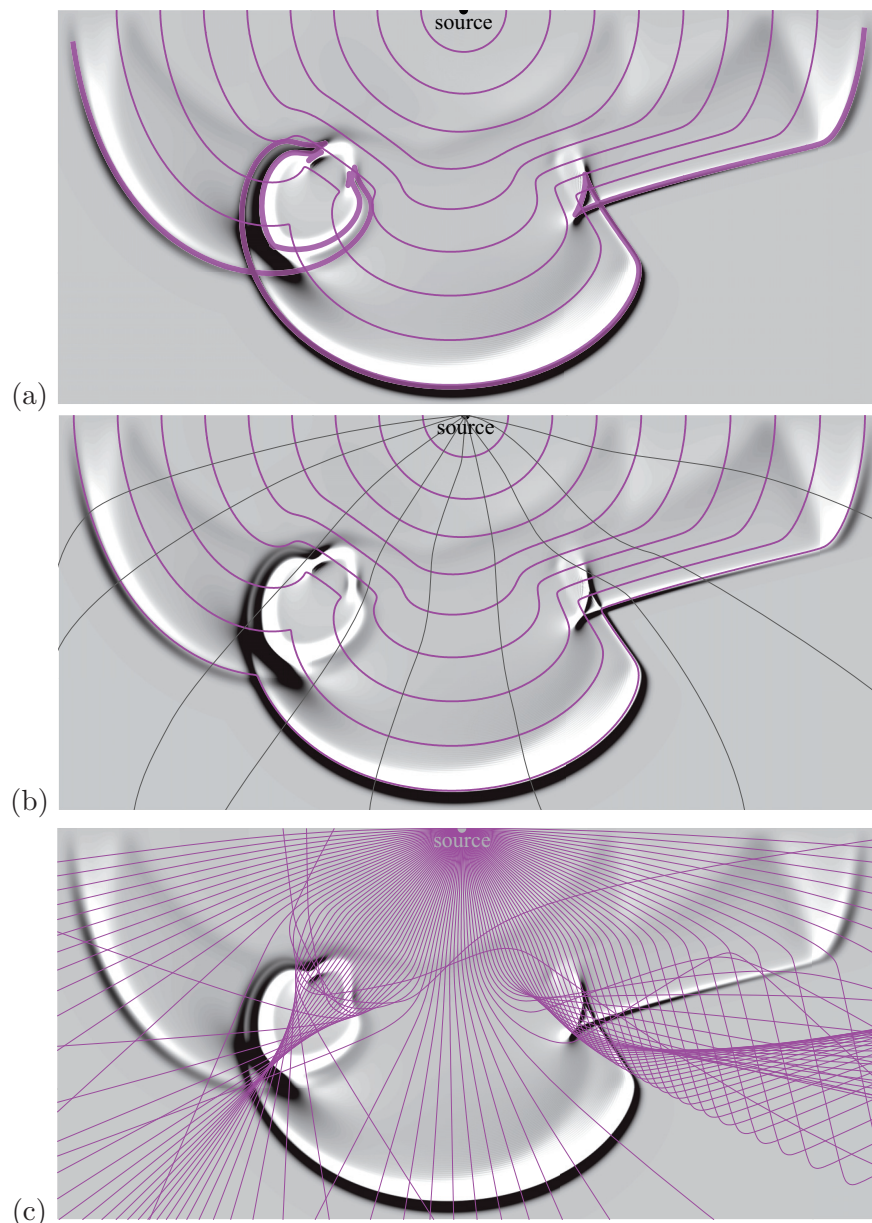


Figure 1. Wave propagation in heterogeneous media with one source of wave propagation. Light to dark background illustrates increasing velocity. (a) Wave front real solution. (b) Eikonal equation solution and the geodesics drawn by back tracing the characteristics. (c) The ray-tracing solution. (Reproduced from [45] by permission.)

the procedure is repeated until a complete path is computed. For some general references on ray-tracing methods, we refer the reader to, e.g., [22, 8, 25, 45, 36, 53]. In the following, we describe the ray-tracing procedure in more detail.

A geodesic connecting a pair of points on a Riemannian manifold minimizes the length

functional (2.1). Let $\mathbf{x} = (x^1, x^2, x^3)^T$ be a point on a geodesic. As we showed in section 2, the minimizer of (2.1) satisfies the system of three second-order ODEs (2.6) with so-called Christoffel symbols defined in (2.5) and (2.7). Let us introduce $u^\gamma(\tau) := \dot{x}^\gamma(\tau)$ for $\gamma = 1, 2, 3$; then we can rewrite system (2.6) as follows:

$$(3.1) \quad \begin{aligned} \dot{x}^\alpha &= u^\alpha, \\ \dot{u}^\alpha &= -\Gamma_{\beta\gamma}^\alpha u^\beta u^\gamma. \end{aligned}$$

Consider a point $(x^1(0), x^2(0), x^3(0))$ as the given initial point in the domain, and $(u^1(0), u^2(0), u^3(0))$ as the initial direction. We compute the solution to (3.1) for the given initial position and multiple initial directions using sophisticated ODE solvers, such as the fourth-order explicit Runge–Kutta method. This gives us a set of geodesics connecting the given initial point to some points on the boundary. In ray-tracing [22, 26, 7], there is no control of where the rays pass through. A common way to obtain a solution from the given initial point to a desired point is to apply two-point ray-tracing; see, e.g., [49, 45, 43]. First, a large number of rays are shot from both points. We continue the integration until rays hit the boundary. This gives us two sets of geodesics that connect each initial position to the boundary. Next, we obtain the geodesics between the two points by postprocessing the geodesics. In applications where the medium is piecewise linear the postprocessing is simplified. This is because rays are straight lines or very smooth. However, the postprocessing becomes computationally expensive when the application involves rays from multiple source points to multiple end points, and the extension to three dimensions is relatively complex. On the other hand, for our specific application, DTI fiber-tracking, calculating the exact connection between two given points is not favored since this is not known. Instead, we prefer the connection between two given regions. Therefore, in this paper we focus on developing ray-tracing for point-region and region-region fiber-tracking.

The computational domain is discretized uniformly with grid size h and grid points $x_{ijk} = (x_i^1, x_j^2, x_k^3) = h(i, j, k)$ for $i = 0, 2, 3, \dots, N - 1$, where N is the number of grid points in each spatial direction. For simplicity we take the number of grid points equal in all directions. We assign to each grid point a 3×3 tensor $G_{ijk} = D_{ijk}^{-1}$. We approximate the derivatives of $g_{\alpha\beta}$ at each grid point by the standard second-order central difference scheme, i.e.,

$$(3.2) \quad \frac{\partial g_{\alpha\beta}}{\partial x^1}(x_i^1, x_j^2, x_k^3) \approx \frac{1}{2h} (g_{\alpha\beta}(x_{i+1}^1, x_j^2, x_k^3) - g_{\alpha\beta}(x_{i-1}^1, x_j^2, x_k^3)).$$

Second-order one-sided differences are applied when the grid points are situated on the boundary, i.e.,

$$(3.3) \quad \frac{\partial g_{\alpha\beta}}{\partial x^1}(x_0^1, x_j^2, x_k^3) \approx \frac{1}{2h} (-3g_{\alpha\beta}(x_0^1, x_j^2, x_k^3) + 4g_{\alpha\beta}(x_1^1, x_j^2, x_k^3) - g_{\alpha\beta}(x_2^1, x_j^2, x_k^3)),$$

$$(3.4) \quad \frac{\partial g_{\alpha\beta}}{\partial x^1}(x_{N-1}^1, x_j^2, x_k^3) \approx \frac{1}{2h} (3g_{\alpha\beta}(x_{N-1}^1, x_j^2, x_k^3) - 4g_{\alpha\beta}(x_{N-2}^1, x_j^2, x_k^3) + g_{\alpha\beta}(x_{N-3}^1, x_j^2, x_k^3)).$$

Note that similar expressions hold for derivatives with respect to x^2 and x^3 . Solving the ODE system (2.4) gives the solution at points that are not necessarily located in the grid points. Therefore, the values of the metric and its derivatives are obtained by applying trilinear interpolation. The integration of geodesics continues until the geodesic hits the boundary of the computational domain.

Initial directions. As mentioned before, in classic ray-tracing we compute the geodesics for the given initial position and a large number of directions densely grouped together. Initial vectors are uniformly distributed using the vertices of regular symmetrical polyhedra [33]. Here all initial vectors are normalized. Astola, Florack, and ter Haar Romeny [1] show that geodesics locally follow trajectories parallel to the direction of the main eigenvalue. However, globally the geodesics are not necessarily parallel to the streamlines obtained by integrating along the main eigenvector direction. This behavior can be exploited to reduce computational time if we assume that the main eigenvector is relatively stable at the initial position. In particular, for DTI fiber-tracking, we can restrict the number of initial shooting directions to an elliptic cone with the largest eigenvalue λ_0 as its axis, and $\lambda_1 R$ and $\lambda_2 R$ as the semimajor axes of the ellipse forming the base of the cone. R is a parameter to control the width of the base. The ellipse constitutes the base of the cone; see Figure 2. Notice that eigenvectors have no sign, so the rays are shot in two directions, and therefore we actually have a double cone. Again here all computed initial directions are normalized. To make the choice of initial directions more reliable, instead of using a constant spread, the elliptic cone could be made dependent on the noise and certainty of the underlying data, similarly to what has been done in probabilistic methods.

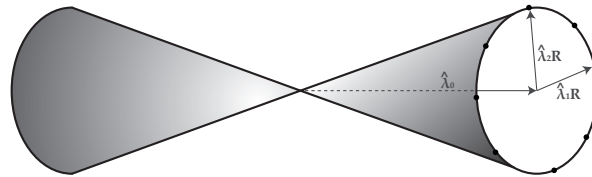


Figure 2. An illustration of the elliptic cone for reducing the number of initial directions. Here R is the radius, and $\hat{\lambda}$ represents the eigenvalue of the tensor at the initial position.

In order to obtain the geodesics of interest with ray-tracing techniques, postprocessing is often desired. A common method is to use the two-point ray-tracing algorithm [36, 43] that was extended to two-dimensional Riemannian DTI space by Sepasian and coworkers [49, 48]. This method computes the multivalued geodesics between two given points inside the domain. Note that finding the exact pathway connecting two given points is not a realistic question for DTI fiber-tracking. It is not possible to know a priori the exact location of the points that are connected. Therefore, we did not further exploit this method. A more realistic approach is to use a point-region or region-region selection. This can be done by selecting two regions of interests which are known to be connected. Geodesics are then started, and filtered by these regions such that they pass through both. Once geodesics are computed, different postprocessing approaches to select the desired geodesic can be applied (see section 4).

3.2. Fast sweeping. For the sake of clarity and better understanding of the differences between the two EL- and HJ-based models, in this section we give a brief review of the numerical method for solving the HJ equation. We present the method used for comparison in this paper. To discretize a general Hamiltonian $H(\mathbf{x}, \mathbf{p})$ several techniques have been developed for both structured and unstructured grids. In this paper we use the Lax–Friedrichs (LF) numerical discretization, proposed by Kao, Osher, and Qian in [23], which satisfies the

required monotonicity and consistency conditions. The major motivation for applying the LF scheme is that an explicit solution formula can always be derived without any assumption on the Hamiltonian.

In order to compute the solution of the discretized eikonal equation, a suitable numerical method needs to be applied. Lenglet et al. [28] and Jbabdi et al. [20] apply fast marching schemes used to determine geodesics and the viscosity solution of the time-dependent HJ equation. Jackowski et al. [19] apply the fast sweeping scheme to estimate the viscosity solution of the stationary HJ equation. In this approach short trajectories that minimize some conformal energy, corresponding to the largest diffusion along the trajectories, are estimated rather than the geodesics. Kao, Osher, and Tsai [24] show that computing the optimized trajectories using the fast sweeping scheme, regardless of discretization, gives the lowest computational complexity. However, Yatziv, Bartesaghi, and Sapiro [58] show that it is also possible to implement the fast marching method with complexity similar to that of fast sweeping. The purpose of our paper is to show the difference between single arrival time solvers and the solvers that compute multivalued solutions such as ray-tracing. Very careful selection of the numerical scheme for solving the HJ equation can lead to a more computationally efficient implementation; see [57]. However, we compute only the first arrival time solution. In this paper we select the fast sweeping scheme for computing the geodesics. Next, we will explain the concept in detail.

We start with the derivation of an explicit formula for the three-dimensional eikonal equation (2.11). First we introduce the difference approximations,

$$(3.5) \quad \begin{aligned} \delta_{x^1} T_{ijk} &:= \frac{1}{2h} (T_{i+1,j,k} - T_{i-1,j,k}), \\ \delta_{x^1 x^1} T_{ijk} &:= \frac{1}{h^2} (T_{i+1,j,k} - 2T_{i,j,k} + T_{i-1,j,k}), \end{aligned}$$

and the averaging operator,

$$(3.6) \quad \mu_{x^1} T_{ijk} = \frac{1}{2} (T_{i+1,j,k} + T_{i-1,j,k}),$$

and likewise for operators in x^2 and x^3 . Here, T_{ijk} is the numerical approximation of $T(x_i^1, x_j^2, x_k^3)$. At each grid point \mathbf{x}_{ijk} we have the following numerical approximation:

$$(3.7) \quad H(\mathbf{x}_{ijk}, \delta_{x^1} T_{ijk}, \delta_{x^2} T_{ijk}, \delta_{x^3} T_{ijk}) - \frac{1}{2} h (\sigma_1 \delta_{x^1 x^1} T_{ijk} + \sigma_2 \delta_{x^2 x^2} T_{ijk} + \sigma_3 \delta_{x^3 x^3} T_{ijk}) = 1.$$

Notice that the only unknown in the equation above is T_{ijk} , which can be isolated to obtain the iterative solver

$$(3.8) \quad \begin{aligned} T_{ijk}^{n+1} &= c (1 - H(\mathbf{x}_{ijk}, \delta_{x^1} T_{ijk}, \delta_{x^2} T_{ijk}, \delta_{x^3} T_{ijk})) \\ &\quad + \frac{1}{2h} c (\sigma_1 \mu_{x^1} + \sigma_2 \mu_{x^2} + \sigma_3 \mu_{x^3}) T_{ijk}, \end{aligned}$$

where

$$c = \frac{h}{\sigma_1 + \sigma_2 + \sigma_3}.$$

Here σ_1 , σ_2 , and σ_3 are the artificial viscosities satisfying

$$\sigma_\alpha \geq \max \left| \frac{\partial H}{\partial p_\alpha} \right| = \max |g^{\alpha\beta} p_\beta|, \quad \alpha = 1, 2, 3.$$

The iteration indices on T_{ijk} in the right-hand side of (3.8) are omitted on purpose, since, depending on the direction of the sweeping, the value will correspond to the previous calculation or the current one. We can show that the monotonicity and convergence of the method are dependent on the appropriate choice of the viscosity terms σ_α for $\alpha = 1, 2, 3$ and on the grid size of the computational domain. We want to keep the viscosity term as small as possible and still have a monotone solution. There are different studies on the appropriate choice of value for σ_α ($\alpha = 1, 2, 3$), and they show that there is a direct relation between convergence rate and the viscosity term. In this paper we choose these values to be 1. More details about the convergence and accuracy of the LF scheme are presented in [24, 61].

We solve the discretized system (3.8) using the fast sweeping method. Fast sweeping relies on the idea of using central finite differences and Gauss–Seidel iteration with alternating sweeping directions. Dividing the characteristics into a finite number of groups according to their direction, the fast sweeping method follows the causality along characteristics. This means that a newly computed value, T_{ijk}^{n+1} , depends on T values in its domain of dependence [24]. In other words, the domain of dependence of the grid point \mathbf{x}_{ijk} is included in the numerical domain of dependence. Values from the previous sweeping step are used to make the error decrease. Therefore, the solution will be updated if and only if $T_{ijk}^{n+1} < T_{ijk}^n$. As the method relies on the fact that by sweeping in different directions, the direction of the characteristic of (2.11) will be eventually followed, there is no need for sorting, in contrast to the fast marching method. The computational complexity of the algorithm is $\mathcal{O}(N^3)$ for a total of N grid points in each direction, and the number of iterations is independent of the grid size [59, 60, 16].

The fast sweeping algorithm consists of the following steps: initialization, alternating sweepings, and enforcing boundary conditions.

Initialization. We assign the exact boundary condition to T_{ijk}^0 at the boundary and keep these values fixed during the iterations. At the interior points we set $T_{ijk}^0 = M$ with M larger than the maximum of the true solutions. These values will be updated in the process of iterations.

Gauss–Seidel alternating sweepings. At iteration $n + 1$, calculate T_{ijk}^{n+1} that solves (3.8). At all grid points \mathbf{x}_{ijk} in the internal domain we carry out the Gauss–Seidel iteration except in those that have a local converged solution value. Recall that this process has to be done in alternating sweeping directions, i.e., in opposite diagonal directions.

Enforcing boundary conditions. After each sweep, we enforce boundary conditions to ensure that characteristics move outside the domain and errors cannot propagate into the domain. Therefore, we have to specify carefully the values of points outside the computational domain, as otherwise huge errors may be introduced and propagate into the computational domain. To tackle this problem, Kao, Osher, and Qian [23] propose the following condition:

$$\begin{cases} u_{0,j,k}^{\text{new}} = \min \left(\max(2u_{1,j,k} - u_{2,j,k}, u_{2,j,k}), u_{0,j,k}^{\text{old}} \right), \\ u_{N-1,j,k}^{\text{new}} = \min \left(\max(2u_{N-2,j,k} - u_{N-3,j,k}, u_{N-3,j,k}), u_{N-1,j,k}^{\text{old}} \right). \end{cases}$$

Note that the same condition can simply be written for other boundaries.

Convergence test. After all the sweepings are performed, check whether

$$(3.9) \quad \|T^{n+1} - T^n\|_{L_1} \leq \epsilon,$$

where $\epsilon > 0$ is the convergence tolerance.

The geodesics for the system described by the Hamiltonian can be obtained by solving the Charpit equations (2.12a)–(2.12c). Notice that the momenta can be computed from the viscosity solution. For this we use the central difference scheme. One can construct the solution for the PDE (2.11) by integrating each one of the equations (2.12a)–(2.12c). Once this step is finished, any point in the domain can be connected by a geodesic to the initial position.

4. Pre- and postprocessing. In the previous sections we described how to compute the geodesics in general. In the following we focus on pre- and postprocessing, suitable for our specific problem.

Preprocessing. All geodesic-based methods allow the geodesics to deviate from the direction of diffusion. This is an advantage because the geodesics become less sensitive to noise, but at the same time they can deviate too much if diffusion profiles are not sharp. In order to deal with this problem, Descoteaux, Lenglet, and Deriche [12] propose tensor sharpening by raising tensors to a certain power, i.e.,

$$D_{\text{sharp}} = D^n, \quad n \in \mathbb{N}.$$

Here D and D_{sharp} are the diffusion tensor and sharpened tensor, respectively. Sharpening the matrix means small eigenvalues will become relatively smaller and large ones will become relatively larger. This method causes the ellipsoid to increase or decrease in volume. To prevent this, one can normalize the tensor using its determinant, which is the same as the product of its eigenvalues. Afterwards, the ellipsoid has to be multiplied by the original determinant to give its volume back, although it is not equal to the volume of the original ellipsoid; thus

$$(4.1) \quad D_{\text{sharp}} = \left(\frac{D}{|D|} \right)^n |D|,$$

with $|D|$ the determinant of the tensor D . Then we have

$$(4.2) \quad |D_{\text{sharp}}| = |D|^{3-2n}.$$

Note that for an m -dimensional matrix, (4.2) is written as the following:

$$(4.3) \quad |D_{\text{sharp}}| = |D|^{n(1-m)+m}.$$

Tensor sharpening diminishes the isotropic part and enhances the dominant eigenvector. However, powering the tensor can introduce other difficulties such as enhancing noise. The proper choice of the exponent n is highly dependent on the data and its orientation, and different values are proposed in the literature [12, 54].

Postprocessing. Once all geodesics are computed either with HJ or ray-tracing, a selection needs to take place. Any two points in the domain can be connected by geodesics, but not all

reflect the underlying fibrous structure. One can measure the strength of geodesics connecting two points by applying a connectivity measure. The connectivity measure is used for finding a suitable trajectory corresponding best to real fiber bundles. We apply these measures in order to discard the geodesics without strong connections between points in the domain. Since the fibers correspond to geodesics that connect a pair of points in the Riemannian manifold, the most reasonable connectivity measure is the one that minimizes trajectories in a Riemannian manifold.

In recent papers, Astola, Florack, and ter Haar Romeny [1] and Parker et al. [41] presented the connectivity measure as the ratio of the geodesic lengths given by the Euclidean and Riemannian metric tensors. This measure can be considered as a measure for the connectivity strength of a geodesic. The proposed measure reads

$$(4.4) \quad m[\chi] = \frac{\int_a^b |\dot{\chi}(\tau)| d\tau}{J[\chi]},$$

with $J[\chi]$ defined in (2.1). Note that locally, in anisotropic voxels, this measure obtains its maximum in the direction of the eigenvector corresponding to the largest eigenvalue; see [1].

5. Results. In this section, we present a feasibility study for the computation of geodesics, for both discrete three-dimensional synthetic tensor fields and real human brain DTI data. We present the results and analyze the behavior of streamline-based methods, the ray-tracing algorithm, and our implementation of the fast sweeping method described in section 3.2.

The behavior of the presented methods is evaluated in fiber structures with high curvature, like U-shaped fibers, and fiber crossings. We use synthetic data sets with a resolution of $20 \times 20 \times 6$. We define the anisotropic region as R_1 and the background as R_2 , and then tensors corresponding to each region are computed with eigenvalues, $\lambda_{R_1} \sim [3 \times 10^{-3}, 17 \times 10^{-4}, 17 \times 10^{-4}]$ mm²/s and $\lambda_{R_2} \sim [7, 7, 7] \times 10^{-4}$ mm²/s. In order to mimic real DTI acquisition, Rician noise is added. The signal attenuation for different gradient directions is obtained using the inverse of the Stejskal–Tanner equation [52]. The noise is then added to the noiseless signal with a signal to noise ratio (SNR) of 15.3, and then the tensors are estimated again.

The evaluation on real data is based on two DTI data sets of healthy volunteers. The first data set, $D1$, was acquired by a 3T Siemens scanner with $256 \times 256 \times 172$ voxels, with resolution $1 \times 1 \times 1$ with a b -value of 1000s/mm² and 72 gradient directions. The second data set, $D2$, was acquired by a Philips scanner, with $128 \times 128 \times 66$ voxels, with resolution $2 \times 2 \times 2$ mm, b -value of 1000s/mm², and 32 gradient directions.

The seed regions are selected manually. In real data they are based on available anatomical atlases. Once the seed region is selected, seed points are generated inside the selected seed region in an arbitrary interval. In ray-tracing, the geodesic is computed by shooting rays from an initial point to all selected directions. After fiber reconstruction, we can select fibers by applying one point-region or region-region fiber-tracking; see section 3.1. Later, one can narrow the geodesics (fibers) that connect the two given regions by applying the connectivity measure.

5.1. Curved fiber reconstruction. In this section, we want to demonstrate that our proposed ray-tracing method is superior to the first arrival solvers method for fiber bundles

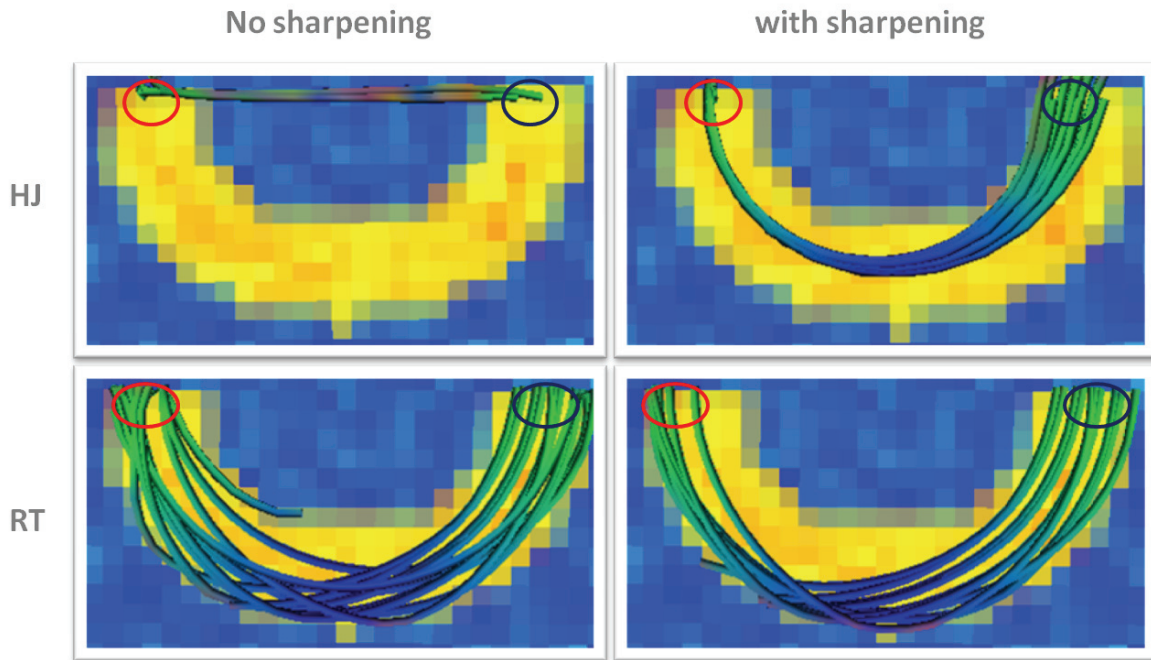


Figure 3. Synthetic data set with the form of a short U-shaped fiber: Geodesics computed for the tensor field with and without sharpening using the ray-tracing method and the HJ equation.

with high curvature, like U-shaped fiber bundles. For this propose we use two different data sets of short and long U-shaped bundles. Figure 3 shows a synthetic data set of a short U-shaped fiber. The background is color coded based on the fractional anisotropy (FA), and fiber tracts are colored using the common RGB color coding of the main eigenvector, \mathbf{e} (i.e., $(R, G, B) = (|e_1|, |e_2|, |e_3|)$). The seed points are indicated by red disks, and the end points by dark blue disks. In the left side of Figure 3 we show the result for both HJ and ray-tracing fiber-tracking using no sharpening. Note the shortcuts obtained using the HJ approach. Here, no segmentation has been used. In the right side of Figure 3 we show the tractography results with the anisotropy enhancement of the tensor using the sharpening factor $n = 2$. We see that applying sharpening improves the front propagation to be faster along the U-fiber than in the background. As a result, the fiber tracts obtained by back tracing the fronts follow the U-fiber. Note that the ray-tracing method gives correct fiber tracts independent of the sharpening.

Figure 4 shows a synthetic data set of a long U-shaped fiber. The seed points and end points are visualized by red disks. We learned from the previous figure that tensor sharpening can improve the front propagation result. Therefore, here for preprocessing of the U-shaped synthetic data we choose the tensor sharpening factor $n = 2$. The fibers are reconstructed by solving the HJ equation with different choices of end points, and by the ray-tracing algorithm. In Figure 4(a), the HJ equation is solved, and it can be seen that the fibers are correctly reconstructed. However, if the end points are set at the other end of the fibers where the reconstructed fibers should have higher curvature (see Figure 4(b)), the fibers actually cross

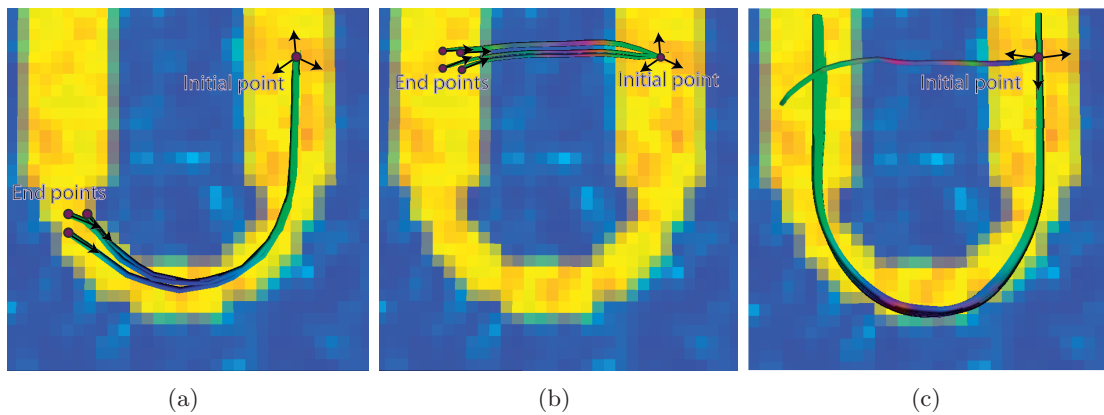


Figure 4. Synthetic data set with the form of a long U-shaped fiber: Geodesics computed using the HJ equation with different choices of end points (a), (b) and the ray-tracing algorithm (c). In all cases the initial value is situated in the same point. The slice is color coded according to the FA with a rainbow color coding: yellow indicates high anisotropy, and blue indicates low anisotropy. The fibers are colored according to the RGB color coding of the main eigenvector.

the isotropic area. The choice of metric has influence on this, as Lenglet et al. [28] have remarked. However, Figure 4(c) shows that with the same choice of metric and minimizing the same functional, capturing the correct geodesic corresponding to the desired fiber bundle is feasible. A heuristic explanation is that the viscosity solution obtained via fast sweeping only gives the solution corresponding to the first arrival time. Since we do not apply any threshold for defining the anisotropic regions for U-fibers, the Riemannian length of the shorter trajectory connecting the two ends of the U will win the cost of the front evolution. We see that in ray-tracing, Figure 4(c), the two possible geodesics starting from the given seed point meet at the same point at the other side of the U-fiber.

In Figure 5, we demonstrate a similar effect for the healthy volunteer DTI data set $D2$. The color codings are the same as those in Figure 4. We illustrate the reconstruction of a few fibers of the corpus callosum bundle. Figure 5(a) is the result of solving the HJ equation by placing the seed and end points in opposite extremes, and it has the same effect as in Figure 4(b). Figure 5(b) illustrates that if the seed and end points are placed such that the individually reconstructed fibers are less curved, the correct result can be achieved. Figures 5(c) and 5(d) show the results using ray-tracing when the seed points and stopping regions are in similar locations as in Figures 5(a) and 5(b), respectively. We can see that, regardless of the position of the initial points, the ray-tracing will result in the correct fiber reconstruction.

5.2. Crossing fiber reconstruction. We also examine the capability of the method for recovering the desired fiber bundle in areas with crossing fibers, i.e., X-fibers. Each line segment along the geodesic curve follows Snell's law (which describes the relation between the angle of incidence and refraction). In addition, each line segment locally follows the direction that satisfies the minimization constraint. In our case, the constraint is that the direction minimizes the path. In the directional domains, the minimum not only depends on the direction of the propagation speed (dominant diffusion direction) but is also influenced by the whole diffusion profile at the point of arrival and the previous direction.

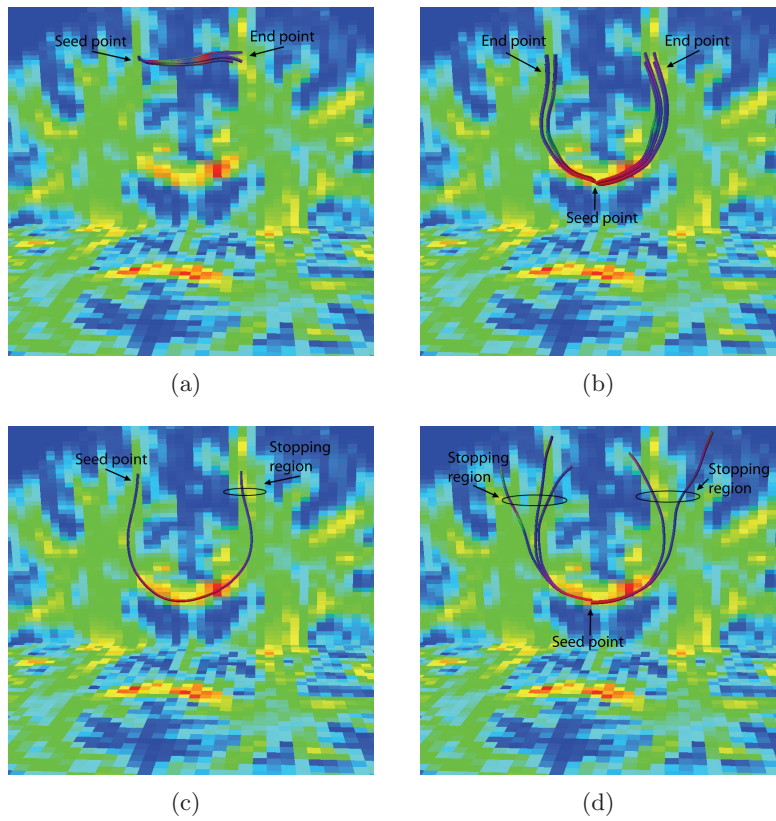


Figure 5. Reconstructing a few fibers of the corpus callosum bundle for the D2 data set, using (a) and (b) an HJ-based algorithm, (c) and (d) a ray-tracing algorithm.

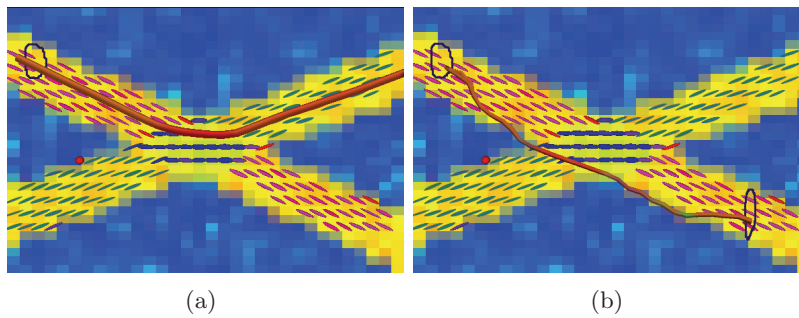


Figure 6. Fiber reconstruction computed using the streamline approach (a) and by solving the HJ equation (b). Note that the front propagation is intrinsically triggered by the diffusion profile. Therefore, the fiber tract is not exactly following the center line of the fiber bundle.

We examine this by an example of a synthetic forty-five degree X-fiber data set. In Figure 6, the X-fiber data set is shown using the same color coding scheme described above. The ellipsoids describing the diffusion profiles at each voxel are also shown. In Figure 6(a), the reconstruction based on the classic streamline fiber-tracking is shown. Note that the fiber

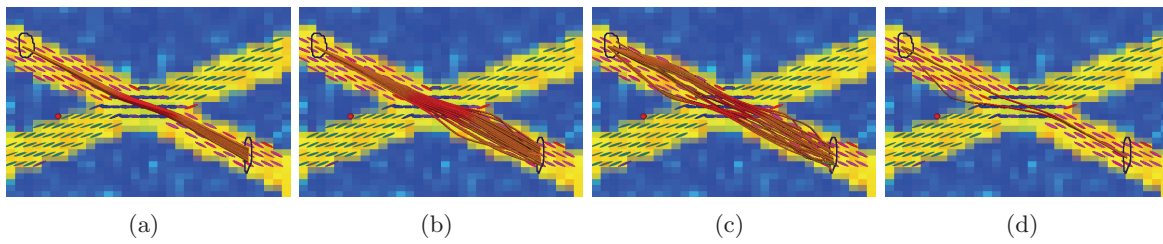


Figure 7. Perturbation of the initial angle around the main eigenvalue of the tensor at the initial position (a) $R = 0.02$, (b) $R = 0.08$, (c) $R = 0.26$, (d) $R = 0.40$.

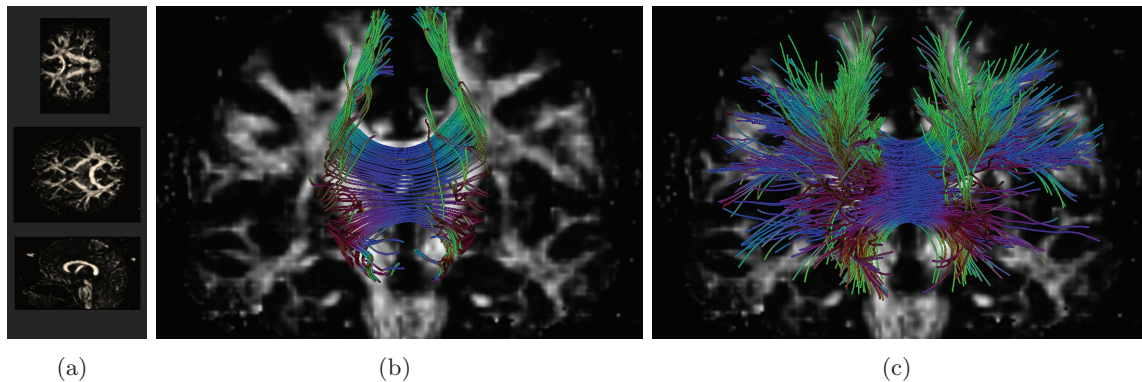


Figure 8. Fiber-tracking results for the corpus callosum, using stream-line (a) or geodesics via the ray-tracing method (b).

changes direction once it meets the crossing area. Figure 6(b) shows the result solving the HJ equation. As expected, the HJ solution gives a structure closer to the expected correct path; however, the path is not straight.

Figure 7 illustrates the computed results for the ray-tracing method. We can observe that the results are closer to the expected fibers than in Figure 6. In order to show the robustness of ray-tracing, we vary the number of shooting directions by varying the density of sampled orientations within the cone as described in section 3.1. In Figure 7 the results are shown for testing the stability of geodesics to small perturbation around the main eigenvalues corresponding to the seed point. To do that we vary the radius of the shooting cone from $R = 0.02$ to 0.4 ; consequently, we also reduce the sampling density of the initial directions. We observe in Figure 7 that the geodesics still follow the desired bundles even with relatively large perturbation.

In the following, we illustrate the behavior of crossing fibers in the real data set $D1$. We reconstruct the corpus callosum around the centrum semiovale, which is the region where the corona radiata bundle and the corpus callosum cross. It is expected that the corpus callosum fibers around this area will diverge and spread towards the cortex. In Figure 8(a), we show orthogonal slices of $D1$ FA map color coded by a gradient from black through brown to white. Figure 8(b) shows the streamline results by seeding within a region of interest around the corpus callosum in the middle sagittal slice. It can be observed that streamlines cannot

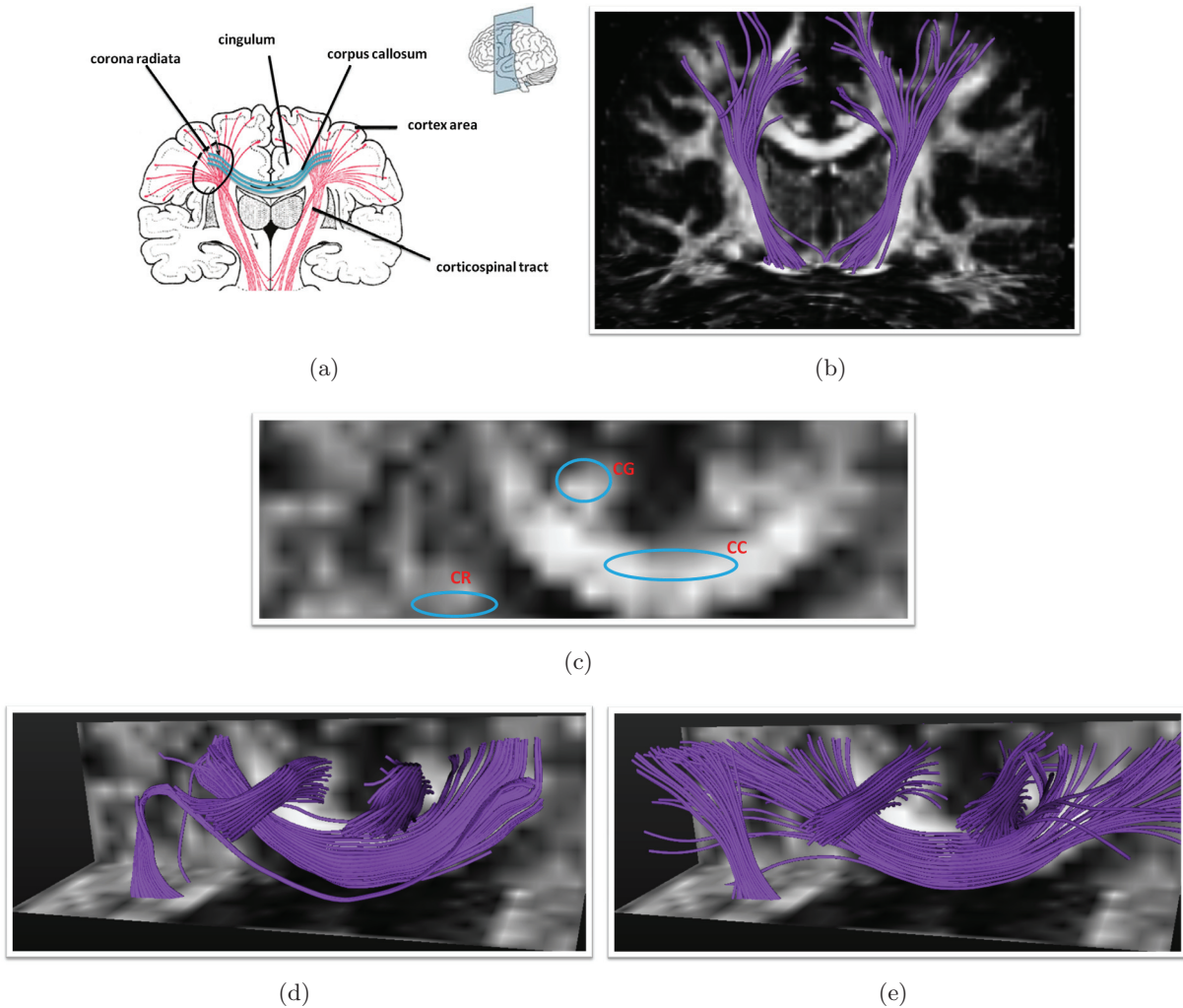


Figure 9. Tractography results for $D2$ in the crossing regions: (a) a sketch illustrating crossing fibers of corona radiata (CR), corpus callosum (CC), and cingulum (CG); (b) corticospinal tracts; (c) the seed regions; (d) streamline tractography (streamlines); (e) ray-tracing tractography.

capture the corpus callosum fiber divergence. In Figure 8(c), we trace geodesics using ray-tracing that starts at the same seed points as in Figure 8(b), sampling directions in a cone around the main eigenvector of each seed point. The tracing is stopped after a finite time, and fibers are selected using the connectivity measure (4.4). It can be observed that these methods comply with the known anatomy of the corpus callosum [35]. Figure 9(b) illustrates the fiber tracts for corticospinal fibers converging to the motor cortex through the corona radiata, analyzed using $D2$ data set. Figures 9(d) and 9(e) show the fiber reconstruction for the crossing regions of the corona radiata (CR), corpus callosum (CC), and cingulum (CG) using a $10 \times 10 \times 30$ cube cut from $D2$. Figure 9(d) shows the result of the streamline-based tractography method. The fiber-tracking stops in voxels with threshold lower than 0.1. Figure 9(e) shows the tractography result for the ray-tracing method. In this figure fibers stop when

Table 1*Computational time for HJ and ray-tracing tractography.*

No. of fibers	Tractography method	Time(s)
300	Fast sweeping	247
300	Ray-tracing	9

they meet one of the boundaries. The initial directions are sampled with small cones around the main eigenvector directions of the corresponding seed points. Note that for the case when the seed points are situated in the crossing area of the corona radiata, it is better to sample the initial directions using the vertices of regular symmetrical polyhedra. Similar to the previous example, notice the capability of ray-tracing method for better reconstruction of the fibers in the crossing area. It is good to mention that this is not possible with streamlines, and that for the HJ approach end points would need to be defined at all corresponding cortex positions. Compared to the HJ approach, in ray-tracing methods the geodesics are directly computed. In the HJ approach, in order to compute the geodesics between an initial point and any other points inside the domain, computation for the whole domain is necessary; once the user needs to change the initial point, the whole computation would have to be repeated. This is because the geodesics are computed implicitly from the fronts. However, in ray-tracing, changing the seed points and computing geodesics for the new seed points can be done in a couple of seconds. For more detailed discussions and results of reconstructing the fibers in the corresponding regions using the HJ approach, we refer the reader to [20, 28, 19, 44].

Table 1 shows the computational time for the HJ and ray-tracing tractography for the fibers originating from a single initial point. Note that in the case of the HJ approach the end points should be defined. For this computation we set the end point on the boundaries. For the ray-tracing method, fibers stop when they meet one of the boundaries. All the computations have been done on a single computer having an Intel dual core central processing unit (CPU) (only one core has been used) with a processor clock rate of 1.86 GHz.

We implemented the existing algorithm on the highly parallel architecture of a graphical processing unit (GPU), using the NVIDIAs Compute Unified Device Architecture (CUDA) programming language [37]. Since fibers can be computed independently of each other, the tractography algorithm can be meaningfully parallelized. As a result, the running time can be reduced by a factor of up to 175 using modern GPU, compared to an implementation on a single-core CPU. The results for this test are shown in Figure 10. For this test we used a real DTI image with dimensions of $128 \times 128 \times 30$ voxels. Seed points were placed in a small, two-dimensional region of 22×4 voxels, located in a part of the corpus callosum. Seed points were randomly placed within this region, with a random initial direction. In order to fully explore the performance gain, we used four different CUDA-supported GPUs. One of the important specification of these GPUs is the memory bandwidth (number of bits which can be pulled from memory per second). The number of seed points varies from 1024 to 4096, which closely mimics a real-life application of the ray-tracing algorithm. For each configuration, we show the running time in seconds and the speed-up factor relative to the CPU implementation. For more detailed information about the implementation and memory management we refer the interested reader to [55].

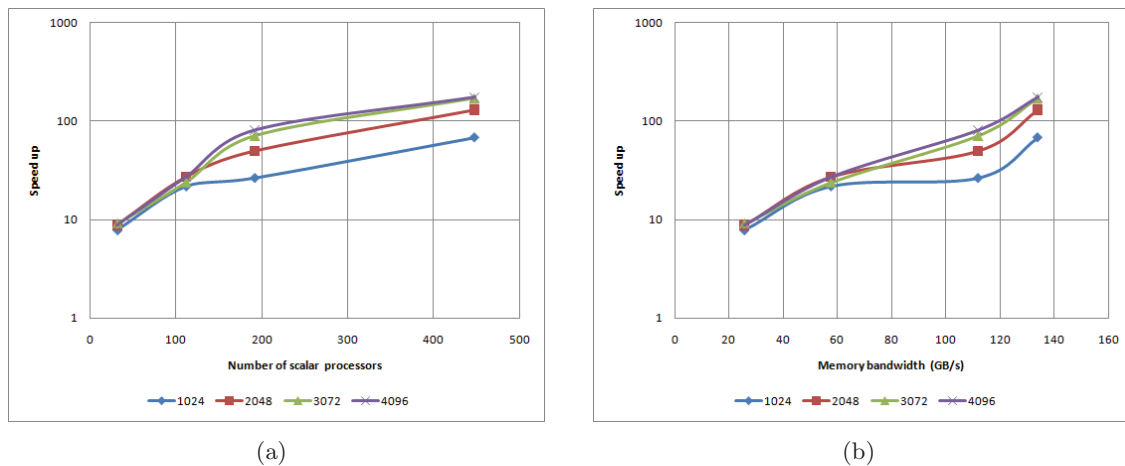


Figure 10. An illustration of the speed-up versus the number of scalar processor for (a) different number of seeds and (b) the memory bandwidth.

6. Conclusions and future work. In this paper, we presented a geodesic-based method for fiber-tracking in diffusion tensor imaging (DTI) data. We derived the Euler–Lagrange geodesic equations for three-dimensional Riemannian space and applied the ray-tracing method to compute the solution. This new algorithm allows us to have more control over local orientation inside the domain and gives multivalued solutions. For comparison, we also discussed a fast sweeping algorithm as an example of a first arrival solver for the stationary HJ equation. This algorithm puts the constraint of the first arrival time and ignores later arrivals. This method and similar approaches are robust to noise. However, they can produce nonphysical solutions, e.g., shortcuts. This can be due to either the computation of only the first arrival time or the choice of the functional to be minimized. It is worthwhile to investigate the behavior of these methods for different functionals. Particularly for DTI, the realistic solution obtained by the first arrival solver highly depends on how realistic the functional is for minimizing the arrival time. For example, if we could derive a functional that could handle all limitations of the data, then we could prevent so many well-known shortcomings of first arrival solvers. However, the derivation of such a functional is still unknown to us. Therefore, it is promising to have a method that suppresses these limitations and instead gives us a wider set of possible geodesics. This can be obtained by looking at all possible solutions instead of only the first arrival times. Furthermore, we are also interested in looking at algorithms that give better insight into the local geometry as well as the global structure of the domain.

Results for realistic synthetic data have been shown for both HJ-based fiber-tracking and the ray-tracing algorithm. We show the potential of the ray-tracing method for capturing the correct tract, especially for U-shaped fibers.

The ray-tracing approach also suffers from some drawbacks. The numerical scheme computes a finite number of rays. When these rays diverge, some regions will be visited by many rays and some by none. Controlling the ray density to achieve roughly uniform sampling of the travel-time is feasible by using computationally expensive interpolation. The challenge is to develop an algorithm which retains the efficiency of modern first arrival time solvers and

at the same time captures all arrival times. In ray-tracing the distribution of fibers is based on the global minimization described by geodesics. As an extension of this research, we are currently investigating the generalization of the ray-tracing algorithm for fiber-tacking to high angular resolution diffusion imaging. Finally, it would be interesting to study the combination of ray-tracing and probabilistic fiber-tracking.

Acknowledgment. The authors would like to thank Olof Runborg for permission to use Figure 1.

REFERENCES

- [1] L. J. ASTOLA, L. M. J. FLORACK, AND B. M. TER HAAR ROMENY, *Measures for pathway analysis in brain white matter using diffusion tensor imaging*, in Proceedings of the 20th International Conference on Information Processing in Medical Imaging, Lecture Notes in Comput. Sci. 4584, Springer, New York, 2007, pp. 642–649.
- [2] P. J. BASSER AND C. PIERPAOLI, *Microstructural and physiological features of tissues elucidated by quantitative-diffusion-tensor MRI*, J. Magnetic Res., 111 (1996), pp. 209–219.
- [3] T. E. BEHRENS, H. J. BERG, S. JBABDI, M. F. RUSHWORTH, AND M. W. WOOLRICH, *Probabilistic diffusion tractography with multiple fibre orientations: What can we gain?*, Neuroimage, 34 (2007), pp. 144–155.
- [4] J. BERMAN, S. CHUNG, P. MUKHERJEE, C. P. HESS, E. T. HAN, AND R. G. HENRY, *Probabilistic streamline q-ball tractography using the residual bootstrap*, Neuroimage, 39 (2008), pp. 215–222.
- [5] M. BJÖRNEMO, A. BRUN, R. KIKINIS, AND C. F. WESTIN, *Regularized stochastic white matter tractography using diffusion tensor MRI*, (2002), pp. 435–442.
- [6] P. BULANT AND L. KLIMEŠ, *Interpolation of ray theory traveltimes within ray cells*, Geophys. J. Internat., 139 (1999), pp. 273–282.
- [7] V. ČERVENÝ, I. A. MOLOTKOV, AND I. PSENCIK, *Ray Method in Seismology*, University of Karlova Press, 1977.
- [8] R. C. Y. CHIN, G. HEDSTROM, AND L. THIGPEN, *Numerical methods in seismology*, J. Comput. Phys., 54 (1984), pp. 18–56.
- [9] P. A. COOK, D. C. ALEXANDER, AND G. J. M. PARKER, *Modelling noise-induced fibre orientation error in diffusion-tensor MRI*, Proc. ISBI, 1 (2004), pp. 332–336.
- [10] P. A. COOK, H. ZHANG, B. B. AVANTS, P. YUSHKEVICH, D. C. ALEXANDER, J. C. GEE, O. CICCARELLI, AND A. J. THOMPSON, *An automated approach to connectivity-based partitioning of brain structures*, in Proceedings of MICCAI 2005, Lecture Notes in Comput. Sci. 3749, Springer, New York, 2005, pp. 164–171.
- [11] M. G. CRANDALL AND P. L. LIONS, *Viscosity solutions of Hamilton-Jacobi equations*, Trans. Amer. Math. Soc., 277 (1983), pp. 1–42.
- [12] M. DESCOTEAUX, C. LENGLET, AND R. DERICHE, *Diffusion tensor sharpening improves white matter tractography*, in Proceedings of SPIE, 6512 (2007), pp. 65121J–65121J-9.
- [13] L. O’ DONNELL, S. HAKER, AND C. F. WESTIN, *New approaches to estimation of white matter connectivity in diffusion tensor MRI: Elliptic PDEs and geodesics in a tensor-warped space*, in Proceedings of MICCAI 2002, Lecture Notes in Comput. Sci. 2488, Springer, New York, 2002, pp. 459–466.
- [14] L. C. EVANS, *Partial Differential Equations*, 19, American Mathematical Society, Providence, RI, 1998.
- [15] B. GEYER, D. M. GITMAN, AND I. V. TYUTIN, *Canonical form of Euler-Lagrange equations and gauge symmetries*, J. Phys. A, 36 (2003).
- [16] P. A. GREMAUD AND C. M. KUSTER, *Computational study of fast methods for the eikonal equation*, SIAM J. Sci. Comput., 27 (2006), pp. 1803–1816.
- [17] H. A. HAROON AND G. J. PARKER, *Using the wild bootstrap to quantify uncertainty in fibre orientations from q-ball analysis*, in Proc. Intl. Soc. Mag. Reson. Med., 15 (2007).
- [18] T. HOSEY, G. WILLIAMS, AND R. ANSORGE, *Inference of multiple fiber orientations in high angular resolution diffusion imaging*, Magn. Reson. Med., 54 (2005), pp. 1480–1489.

- [19] M. JACKOWSKI, C. Y. KAO, M. QUI, R. T. CONSTABLE, AND L. H. STAIB, *White matter tractography by anisotropic wavefront evolution and diffusion tensor imaging*, *Medical Image Anal.*, 9 (2005), pp. 424–440.
- [20] S. JBABDI, P. BELLEC, R. TORO, J. DAUNIZEAU, M. PÉLÉGRINI-ISSAC, AND H. BENALI, *Accurate anisotropic fast marching for diffusion-based geodesic tractography*, *Int. J. Biomed. Imaging*, 2008 (2008), pp. 1–12.
- [21] B. JEURISSEN, A. LEEMANS, D. K. JONES, J. TOURNIER, AND J. SIJBERS, *Probabilistic fiber tracking using the residual bootstrap with constrained spherical deconvolution*, *Human Brain Mapping*, (2010).
- [22] B. R. JULIAN AND D. GUBBINS, *Three-dimensional seismic ray tracing*, *J. Geophys. Res.*, 43 (1977), pp. 95–114.
- [23] C. Y. KAO, S. OSHER, AND J. QIAN, *Lax-Friedrichs sweeping scheme for static Hamilton-Jacobi equations*, *J. Comput. Phys.*, 196 (2004), pp. 367–391.
- [24] C.-Y. KAO, S. OSHER, AND Y.-H. TSAI, *Fast sweeping methods for static Hamilton-Jacobi equations*, *SIAM J. Numer. Anal.*, 42 (2005), pp. 2612–2632.
- [25] S. KIM AND R. COOK, *3-D travelttime computation using second-order ENO scheme*, *Geophys.*, 64 (1999), pp. 1867–1876.
- [26] R. T. LANGAN, I. LERCHE, AND R. T. CUTLER, *Tracing of rays through heterogeneous media: An accurate and efficient procedure*, *Geophys.*, 50 (1985), pp. 1456–1465.
- [27] A. LENGLET, R. DERICHE, AND O. FAUGERAS, *Inferring white matter geometry from diffusion tensor MRI: Application to connectivity mapping*, in *Proceedings of the Eighth European Conference on Computer Vision*, *Lecture Notes in Comput. Sci.* 3021–3024, Springer, New York, 2004, pp. 127–140.
- [28] C. LENGLET, E. PRADOS, J.-P. PONS, R. DERICHE, AND O. FAUGERAS, *Brain connectivity mapping using Riemannian geometry, control theory, and PDEs*, *SIAM J. Imaging Sci.*, 2 (2009), pp. 285–322.
- [29] T. MA AND H. D. TAGARE, *Consistency and stability of active contours with Euclidean and non-Euclidean arc-lengths*, *IEEE Trans. Image Process.*, 8 (1999), pp. 1549–1559.
- [30] C. MANTEGAZZA AND A. C. MENNUECCI, *Hamilton-Jacobi equations and distance functions on Riemannian manifolds*, *Appl. Math. Optim.*, 47 (2002), pp. 1–25.
- [31] R. M. M. MATTHEIJ, S. W. RIENSTRA, AND J. H. M. TEN THIJSE BOONKAMP, *Partial Differential Equations: Modeling, Analysis, Computation*, *Math. Model. Comput.* 10, SIAM, Philadelphia, 2005.
- [32] J. MELONAKOS, V. MOHAN, M. NIETHAMMER, K. SMITH, M. KUBICKI, AND A. TANNENBAUM, *Finsler tractography for white matter connectivity analysis of the singulum bundle*, in *Proceedings of MICCAI 2005*, *Lecture Notes in Comput. Sci.* 3749, Springer, New York, 2007.
- [33] E. N. MILLER, *Icosahedra constructed from congruent triangles*, *Discrete Comput. Geom.*, 24 (2006), pp. 437–451.
- [34] S. MORI, B. J. CRAIN, V. P. CHACKO, AND P. C. M. VAN ZIJL, *Three-dimensional tracking of axonal projections in the brain by magnetic resonance imaging*, *Ann. Neurol.*, 45 (1999), pp. 265–269.
- [35] S. MORI, S. WAKANA, P. VAN ZIJL, AND L. M. NAGAE-POETSCHER, *MRI Atlas of Human White Matter*, Elsevier, Berlin, 2005.
- [36] M. MOTAMED AND O. RUNBORG, *A fast phase space method for computing creeping rays*, *J. Comput. Phys.*, 219 (2006), pp. 276–295.
- [37] NVIDIA, *CUDA Programming Guide*, v. 4.1, 2011.
- [38] S. OSHER, *A level set formulation for the solution of the Dirichlet problem for Hamilton-Jacobi equations*, *SIAM J. Math. Anal.*, 24 (1993), pp. 1145–1152.
- [39] G. J. M. PARKER AND D. C. ALEXANDER, *Probabilistic Monte Carlo based mapping of cerebral connections utilising whole-brain crossing fibre information*, *Inf. Proc. Med. Imaging*, 18 (2003), pp. 684–695.
- [40] G. J. M. PARKER AND D. C. ALEXANDER, *Probabilistic anatomical connectivity derived from the microscopic persistent angular structure of cerebral tissue*, *Philos. Trans. R. Soc. Lond. Ser. B Biol. Sci.*, 360 (2005), pp. 893–902.
- [41] G. J. PARKER, D. M. MORRIS, AND K. V. EMBLETON, *Probabilistic fibre tracking: Differentiation of connections from chance events*, *NeuroImage*, 42 (2008), pp. 1329–1339.
- [42] G. J. M. PARKER, C. A. M. WHEELER-KINGSHOTT, AND G. J. BARKER, *Distributed anatomical brain connectivity derived from diffusion tensor imaging*, in *Proceedings of the 17th International Conference on Information Processing in Medical Imaging*, *Lecture Notes in Comput. Sci.* 2482, Springer, New York, 2001, pp. 106–120.

- [43] V. PEREYRA, W. H. K. LEE, AND H. B. KELLER, *Solving two-point seismicray tracing problems in a heterogeneous medium*, Bull. Seismol. Soc. Amer., 70 (1980), pp. 79–99.
- [44] E. PRADOS, S. SOATTO, C. LENGLET, J. P. PONS, N. WOTAWA, R. DERICHE, O. FAUGERAS, AND S. SOATTO, *Control theory and fast marching techniques for brain connectivity mapping*, in Proceedings of the IEEE Conference on Computer Vision and Pattern Recognition, IEEE Computer Society Press, Piscataway, NJ, 2006, pp. 1076–1083.
- [45] O. RUNBORG, *Mathematical models and numerical methods for high frequency waves*, Comm. Comput. Phys., 2 (2007), pp. 827–880.
- [46] H. RUND, *The Hamilton-Jacobi Theory in the Calculus of Variations: Its Role in Mathematics and Physics*, D. Van Nostrand, London, New York, 1966.
- [47] A. RUTHERFORD, *Vectors, Tensors and the Basic Equations of Fluid Mechanics*, 1990.
- [48] N. SEPASIAN, J. H. M. TEN THIJE BOONKAMP, A. VILANOVA, AND B. M. TER HAAR ROMENY, *Multi-valued geodesic based fiber tracking for diffusion tensor imaging*, in Proceedings of MICCAI 2009, Diffusion Modeling and the Fiber Cup Workshop, Lecture Notes in Comput. Sci. 5761, Springer, New York, 2009, pp. 6–13.
- [49] N. SEPASIAN, A. VILANOVA, L. M. J. FLORACK, AND B. M. TER HAAR ROMENY, *A ray tracing method for geodesic based tractography in diffusion tensor*, in Proceedings of the Workshop on Mathematical Methods in Biomedical Image Analysis (MMBIA), IEEE Computer Society Press, Piscataway, NJ, 2008, pp. 1–6.
- [50] J. A. SETHIAN AND A. VLADIMIRSKY, *Ordered upwind methods for static Hamilton-Jacobi equation*, Proc. Natl. Acad. Sci. USA, 98 (2001), pp. 11069–11074.
- [51] K. K. SEUNARINE, P. A. COOK, M. G. HALL, K. EMBLETON, G. J. M. PARKER, AND D. C. ALEXANDER, *Exploiting peak anisotropy for tracking through complex structures*, in Proceedings of the Workshop on Mathematical Methods in Biomedical Image Analysis (ICCV2007), Lecture Notes in Comput. Sci. 3749, Springer, New York, 2007, pp. 1–8.
- [52] E. O. STEJSKAL AND J. E. TANNER, *Spin diffusion measurements: Spin echoes in the presence of a time-dependent field gradient*, J. Chem. Phys., 42 (1965), pp. 288–292.
- [53] C. H. THURBER AND W. L. ELLSWORTH, *Rapid solution of ray tracing problems in heterogeneous media*, Bull. Seismol. Soc. Amer., 70 (1980), pp. 1137–1148.
- [54] J. D. TOURNIER, F. CALAMANTE, D. G. GADIAN, AND A. CONNELLY, *Diffusion-weighted magnetic resonance imaging fibre tracking using a front evolution algorithm*, Neuroimage, 20 (2003), pp. 276–288.
- [55] E. VAN AART, *GPU-Based Acceleration of a Novel Fiber Tracking Algorithm for Diffusion Tensor Imaging Using NVIDIA's CUDA*, Master's Thesis, Eindhoven University of Technology, 2010; <http://alexandria.tue.nl/extra1/afstversl/wsk-i/aart2010.pdf>.
- [56] V. J. WEDEEN, T. L. DAVIS, R. M. WEISSKOFF, R. TOOTELL, B. R. ROSEN, AND J. W. BELLIVEAU, *White matter connectivity explored by MRI*, in Proceedings of the First International Conference for Functional Mapping of the Human Brain, 1995.
- [57] T. XIONG, M. ZHANG, Y. ZHANG, AND C. W. SHU, *Fast sweeping fifth order WENO scheme for static Hamilton-Jacobi equations with accurate boundary treatment*, J. Sci. Comput., 45 (2010), pp. 514–536.
- [58] L. YATZIV, A. BARTESAGHI, AND G. SAPIRO, *$O(n)$ implementation of the fast marching algorithm*, J. Comput. Phys., 212 (2001), pp. 393–399.
- [59] Y. T. ZHANG, H. K. ZHAO, AND S. CHEN, *Fixed-point iterative sweeping methods for static Hamilton-Jacobi equations*, Methods Appl. Anal., 13 (2006), pp. 299–320.
- [60] H.-K. ZHAO, *A fast sweeping method for eikonal equation*, Math. Comput., 74 (2003), pp. 603–627.
- [61] P. ZHU AND S. ZHOU, *Relaxation Lax-Friedrichs sweeping scheme for static Hamilton-Jacobi equations*, Numer. Algorithms, 54 (2010), pp. 325–342.